Simulation study of field-induced morphological changes in a proton-conducting ionomer

Elshad Allahyarov
Department of Physics, Case Western Reserve University, Cleveland, Ohio 44106, USA;
OIVTRAN, Joint Laboratory of Soft Matter, Moscow 127412, Russia;
and HHU Düsseldorf, Institut für Theoretische Physik II, Universitätstraße 1, 40225 Düsseldorf, Germany

Philip L. Taylor
Department of Physics, Case Western Reserve University, Cleveland, Ohio 44106, USA

Hartmut Löwen
HHU Düsseldorf, Institut für Theoretische Physik II, Universitätstraße 1, 40225 Düsseldorf, Germany
(Received 10 November 2009; revised manuscript received 24 January 2010; published 29 March 2010)

A simulation study was made of the effects of strong electric fields on the morphology of a Nafion®-like ionomer at various levels of hydration. The results of united-atom molecular-dynamics computations showed a self-organization of the side chain terminal groups into cylindrical clusters. The walls of these clusters contain the sulfonate dipoles, while the interior holds the majority of the water molecules. These cylindrical structures then align to form an hexatic array aligned along the direction of the applied electric field. The hexatic morphology persists after the removal of the field. A calculation by means of the Kirkwood coupling parameter method shows the Helmholtz free energy of the hexatic morphology of the poled membrane to be lower than that of the initial isotropic material, even in the absence of the applied field.

DOI: 10.1103/PhysRevE.81.031805 PACS number(s): 61.41.+e, 82.47.Nj, 64.75.St, 82.47.Gh

I. INTRODUCTION

Ionomers are used as a gas separator and as conducting material in polymer electrolyte membrane (PEM) devices such as fuel cells [1]. The proton conductivity of a PEM depends on the partial microphase separation of the hydrated membrane into hydrophilic and hydrophobic regions, and the diffusivity of dissociated protons in the hydrophilic domains. Nafion® has been the ionomer most extensively studied, and is considered a good starting point for the development of next-generation polymer electrolytes. Its hydrophobic polytetrafluoroethylene (PTFE) backbone supports fluorinated pendant side chains that are terminated by strongly acidic hydrophilic head groups. The complex diblock copolymeric structure of Nafion facilitates phase segregation in the presence of water. Under equilibrium conditions the terminal groups of the side chains form clusters or larger aggregates interconnected by channels. The geometry of the hydrophilic region is very important for effective operation of a fuel cell, as it is the domain where the protons collectively diffuse from the anode to the cathode.

X-ray scattering studies initially led to a model for the internal morphology of the membrane based on a hydrophilic region consisting of clusters of ionic groups in a reverse micellar structure connected by small channels [2,3]. This model was studied in a number of theoretical investigations for the microphase separation in PEM membranes [3,4]. While the reverse micellar model was accepted through much of the 1990s, later small-angle neutron scattering and small-angle x-ray studies led to a different model consisting of fibrillar aggregates of hydrophobic polymer with the hydrophilic side chains protruding radially outward [5–9]. These hydrophilic regions then constitute irregular channels that can grow or shrink depending on the water content. An alternative model of water channels inside cylindrically inverted micelles was proposed in Ref. [10]. While the Eisenberg model [4] proposes channels connecting hydrophilic regions as an *ad hoc* addition to explain the conduction of protons through the membrane, the fibrillar model [5] and the inverted cylinder model [10] unambiguously result in the existence of channels. Recent molecular-dynamics (MD) simulations of the structure of Nafion have provided additional support for a random structure of interconnected channels [11,12].

The conductivity of ionomers depends strongly on the existence of a continuous hydrophilic pathway in the membrane, and there are on-going efforts to increase the ionomer conductivity by initiating an artificial ordering in its structure. In Ref. [13], a polymer electrolyte was confined in nanopores in a PTFE plate. The authors showed that the conductivity perpendicular to the membrane surface increased as the pore size became smaller. In the smaller pores, the backbone of the polymer electrolyte tended to be parallel to the cylinder surface of the nanopore. Although no information was available for the side chain orientation in the polymer electrolyte used in Ref. [13], it was assumed that alignment in the backbone affects the clusterings of side chains, and thus facilitates proton transfer along the pore axis.

In Ref. [14], a polymer electrolyte was embedded with ion-exchange particles randomly distributed in the polymer matrix. It was found that the application of an alternating electric field during curing of the polymeric matrix resulted in the agglomeration of the added particles in long linear chains extending across the membrane. As a result, the percolation threshold for ion conductance was reduced to be only 0.2–0.3 of its value in membranes with randomly distributed particles. The aligned particles, together with the hydrophilic part of polymer electrolyte, form an efficient pathway for protons.

Lin and co-workers [15] investigated the morphological changes that occur when Nafion is poled in a strong electric field. In order to decrease the backbone viscosity and increase the flexibility of the side chains, the poling was performed on solvent-cast Nafion at temperatures above its glass transition T_g. When the membrane was quenched back to room temperature it retained induced cylindrical aggregates of sulfonates. In Refs. [16,17] it was shown that the poling of Nafion at the membrane-electrode interface above T_g can lead to the formation of chains of carbon-black particles perpendicular to the membrane surface. This is a route to forming improved electrodes for fuel cells.

These promising experimental results suggest the need for simulation studies that might throw light on the microscopic processes involved in these morphological changes. Unfortunately, direct MD simulations of large systems including water evaporation and membrane annealing procedures is beyond the reach of current MD techniques. An alternative path is a route where the temperature, water content, and system volume are kept constant, but in which the strength of the applied field is increased beyond the typical values achievable in experiments. The high fields reduce the activation barrier for molecular motion, and have an effect on Arrhenius factors similar to that of the increase in temperature that occurs during annealing.

This paper is an extension of our previous paper [18] in which MD simulations with implicit solvent were used to investigate nanophase separation in PEM materials under nonequilibrium conditions. In Ref. [18], we demonstrated the advantages of using external fields for inducing ordered morphological changes in PEM membranes. Our findings concerned morphological changes in poled Nafion-like ionomers: in particular, self-organization is found of the terminal groups into cylindrical clusters that resemble the inverted cylinders proposed in Ref. [10]. In the current, more extensive study we treat the absorbed solvent molecules explicitly and analyze the stability of induced structures for three different levels of membrane hydration. We again find hexatic ordering of hydrophilic cylinders in the plane perpendicular to the applied field, and thus show this phenomenon to be to some extent model independent. We extend our study by investigating the reasons that this structure remains in existence when the external field is removed. A free-energy analysis for hydrated membranes with explicit water confirms that the poled membrane structure is more stable than the initial membrane was prior to the poling treatment. The induced agglomeration of hydrophilic head groups, water molecules and protons into long rods reduces drastically the percolation threshold for ion conductance [15]. Thus the formation of rodlike ordered structures in ionomers can be assumed as an initial step in the development of PEM membranes with reduced water content and with a low percolation threshold.

The paper is organized as follows. In Sec. II we discuss the concept of a drift current in PEM membranes under fuel-cell conditions for conductivity measurements. Our united-atom model and simulation details are outlined in Sec. III. Section IV is devoted to simulation results, where we discuss the membrane characteristics under equilibrium and nonequilibrium conditions, morphological changes induced by an applied electric field, and the diffusion of protons. Our free-energy calculations for different membrane morphologies are included in Sec. V. We conclude in Sec. VI.

II. PRACTICALITIES OF PEM MEMBRANE USE

In fuel-cell operation, the anode and cathode are fed by H_2 and O_2 gases. The protons, a product of the catalytic splitting of hydrogen on the anodic side, gradually accumulate at the anode-membrane interface. From there they make reversible transitions into the electrolyte across the so-called inner or Stern layer, which extends a short distance (less than a nanometer) from the electrode surface [19] and develops strong fields, $E \approx 10^6 - 10^7$ kV/m. The charge density at the edge of the inner layer depends on the current demand and the influx rate of hydrogen. A net flow of protons through the membrane is driven by the departure of the concentrations of protons on each side of the inner layer from their equilibrium values [20] and by the gradient $\nabla\varphi(r)$ in the electrostatic potential within the inner layer. The last term also acts on the membrane charges and water molecules absorbed by the membrane. Beyond the inner layer lies the diffuse layer, in which the current of protons is determined self-consistently by the gradients in proton density and electrostatic potential. Within the diffuse layer, the concentration gradient decreases rapidly with distance from the electrode with a decay length that is typically a few nanometers [21], and which depends on the ambient temperature T and the sulfonate concentration n_S. Beyond the diffuse layer the concentration gradient of protons is small [21] and so the concentration of protons differs little from the concentration of sulfonates n_S. In this region the electrostatic field in the bulk polymer, $E=-\nabla\varphi(r)$, is roughly constant [22], and generates a drift current of protons $\vec{j}$ through the membrane. The consequent voltage drop across the electrolyte reduces the potential difference at the electrodes from its maximal value of about 1.1 V for thin Nafion films.

Because we are attempting to predict proton conductivities in PEM materials, it is relevant to consider the methods used to determine this property. The scalar conductivity χ is defined by the relationship

$$\vec{j} = \chi \vec{E}, \tag{1}$$

which relates the electrical current density $\vec{j}$ to the applied field $\vec{E}$. This field can be either constant or alternating [23] and the phenomenon of electro-osmotic drag of water molecules can contribute to the frequency dependence of χ [24,25]. In computer simulations, the membrane conductivity χ is calculated using nonequilibrium molecular-dynamics (NEMD) techniques. In these studies, an electric field is applied to a sample subject to periodic boundary conditions and the resulting current of protons is analyzed. A constant field is used, as the effects that lead to frequency variation of the conductivity at megahertz frequencies are not relevant to simulations that span a time range of the order of nanoseconds.

In our simulations, the proton current density $\vec{j}$ is evaluated as

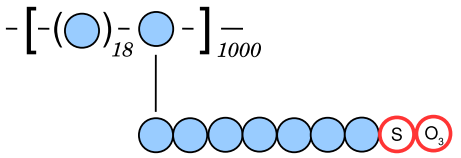

FIG. 1. (Color online) This figure shows a representation of the ionomer model used in the united-atom molecular-dynamics simulations. The shaded particles are electrostatically neutral and hydrophobic, while the unshaded particles with inscribed letters (S for the sulfur atom and O_3 for the oxygen group) are charged and hydrophilic. There are nine united-atom monomers per side chain, 18 backbone monomers per repeat unit, and 1000 repeat units in the simulation box.

$$\vec{j} = (1/V)\sum_{i=1}^{N_S} q_i \vec{v}_{i,z}. \tag{2}$$

Here $v_{i,z}$ is the component of the velocity of the i-th ion along the z axis of the simulation box, which is the direction of the applied field, N_S is the total number of protons in the simulated system, V is the system volume, and q is the charge of the proton. The conductivity χ of the membrane is then found by combining Eqs. (1) and (2).

III. SIMULATION DETAILS

We employ an atomistic approach for a Nafion-like ionomer in the framework of the united-atom representation for the CF_2 and CF_3 groups [26,27], for the sulfur atom S and for the oxygen group O_3 of sulfonates [28]. All united-atom groups are modeled as Lennard-Jones (LJ) monomers having a diameter σ=0.35 nm and an interaction parameter ε_{LJ} =0.2 kcal/mol. The hydrophilicity and hydrophobicity of interactions between united-atom groups are modeled using LJ potentials with modified attractive and repulsive parts [28]. Our approach differs from the mesoscale approximation in which the entire side chain is replaced by a single large hydrophilic blob [12,29–31]. While that drastic approximation made it possible to simulate very large systems, the results obtained are not characteristic of most ionomers. In particular, the diffusion of particles through the membrane is not well represented [32].

In our model, schematically illustrated in Fig. 1, there are nine united-atom monomers per side chain, with the first seven of them being hydrophobic. The last two units, which represent the sulfonate group, are hydrophilic [33]. The charge distribution adopted for the side chains is to place a charge of $+1.1e$ on each sulfur atom (with e the positive charge of a proton) and a charge of $-2.1e$ on each unit representing a group of three oxygen atoms, such that the total charge of a single sulfonate head group SO_3^- is $-e$. The partial charges for the remaining side chain monomers and fluorocarbon groups of the backbone skeleton are set to zero. The hydrogen ions H^+ are considered as units of charge $+e$ and size σ=0.35 nm, interacting electrostatically with the charged monomers of the membrane and the absorbed water. The water molecules were simulated using the TIP3P liquid model [34]. The total interaction potential in the membrane is a combination of electrostatic Coulomb interactions between charged pairs and the 12–6 LJ interactions between all monomers. The ionomer constituents are additionally subjected to stretching, bending, and dihedral forces. The force field implemented, details of which are given elsewhere [35], agrees in most instances with the Nafion model of Paddison [33].

Simulation runs were carried out for three different hydration levels, characterized by values of λ=1, 3, and 5, with λ defined as the number of water molecules per sulfonate group in the membrane. The total simulated system consisted of N_S side chain segments, each terminating in the sulfonate dipole, attached to a long backbone chain, N_p=N_S protons, and λN_S water molecules, each consisting of three charged particles. The total number of charged particles in the simulation box was thus $3(\lambda+1)N_S$. For the case of N_S=1000, considered in this work, there were 18 000 charged particles in the simulation box for the hydrated membrane with λ=5. The rest of the total 44 600 monomers represented the hydrophobic segments of the side chains and backbone of the membrane. There were on average 19 backbone monomers between adjacent side chains. There was a random distribution of side chains along the backbone of the membrane, with a lower limit of 14 backbone monomers and an upper limit of 24 backbone monomers between adjacent side chains. We note that, unlike the case of all-atomistic simulations, which are usually limited to systems containing only a few separate Nafion oligomers with a handful of side chains [26,36,37], in our simulations the backbone is a very long chain with about a thousand attached side chains.

The numerical part of our study consists of three series of production runs. In the first series, a PEM membrane is created and subsequently equilibrated in runs of 100 ps duration at constant volume and temperature. The necessary statistics on the membrane structure and its dynamics were gathered during the following 5 ns. For the second series of runs we imposed an external electric field on the membrane along its z direction. This poling field acted on the head-group monomers of the side chains, on the water molecules, and on the protons in the membrane. During the following 5–10 ns, a change in membrane morphology was generally observed to occur. This morphology gradually reached a steady state, as monitored by the calculation of the potential energy of the ionomer. Once the drift currents of protons and water molecules through the membrane had been stabilized, we gathered statistics during the next 5 ns. In the third series of simulations, we removed the poling E field from the membrane and ran until the entire system reached a steady state. Relaxation from the field-induced morphology back to a field-free equilibrium appeared rapid, typically taking only a couple of nanoseconds. Then, during the following 5 ns, we investigated the statistical and dynamical properties of the relaxed, poled ionomer.

Upon completion of these simulations, we compared the morphology and conductivity of the initial membrane with those of the poled material. In the following account, we refer to the unpoled initial material as membrane I, the membrane in the presence of the poling field as membrane II, and the relaxed membrane after removal of the field as membrane III. During all the runs, the simulated system was

coupled to a Langevin thermostat with a friction coefficient $\gamma=2$ ps^{-1} and a Gaussian white-noise force of strength $6k_BT\gamma$. In the NEMD simulations of the membrane in the poling field, we used friction coefficients in the range of 2 ps$^{-1}\leq\gamma\leq 5$ ps^{-1} for protons and head groups to keep their temperature constant. The equations of motion were integrated using the velocity Verlet algorithm with a time step of 0.5 fs. The time step was halved for strong-field simulations. Standard periodic boundary conditions were imposed on the system by filling space with translational replicas of the fundamental cell. The long-range electrostatic interactions were handled using the standard Lekner summation algorithm [38].

IV. SIMULATION RESULTS

In this section, we present the results for membranes I, II, and III, and also analyze the extent to which the morphologies attained depend on the level, λ, of hydration. In order to accelerate the approach to a local equilibrium of the initial membrane, we temporarily detached the side chains from the backbone skeleton [39] and cut the backbone into 14-monomer segments [40]. After equilibrating runs of 50 ps, the polymer was reassembled and equilibrated with another 100 ps run [18,35]. Statistically averaged quantities were gathered during the following 5–10 ns. The ionomer undergoes a partial phase separation on the nanometer scale into a polymer phase consisting of backbone with pendant side chains and a hydrophilic phase formed by loosely connected clusters of the sulfonate head groups.

A. Hydrated membrane in equilibrium (membrane I)

A typical example of an equilibrated, hydrated membrane with a water content $\lambda=5$ is shown in Fig. 2. The sulfonates, shown as spheres, assemble to form multiplets and clusters of different shapes and sizes. The network of interconnected clusters creates a continuous hydrophilic phase, as expected from the experimental [41–43] and theoretical [12] evidence that the percolation limit for Nafion occurs at $\lambda=2-3$. The coexisting hydrophobic polymer phase is formed by the backbone matrix of the membrane and the hydrophobic parts of the pendant side chains.

To characterize the morphologies of the ionomers simulated, we noted the locations of the sulfur atoms that form part of the sulfonate groups. The more numerous water molecules and the protons are found in association with the sulfonates, and so can be assumed to lie in similarly shaped regions. We find the sulfonates to gather in multiplets of around 10–20 units and that these multiplets in turn form hydrophilic clusters in structures whose character changed with the amount of water present. Calculated sulfur-sulfur pair-correlation functions $g_{SS}(r)$ for different λ are presented in Fig. 3. The peaks in $g_{SS}(r)$ are a convenient measure of the underlying correlation between the head-group positions. It is evident that the strength of spatial correlations between sulfonates depends on the hydration parameter λ, with the most pronounced correlations occurring at low water contents. This trend is a direct consequence of the strong screening of the Coulomb interactions by the water in the membrane. Our results for $g_{SS}(r)$ are in good qualitative agreement with the results of atomistic simulations of Refs. [11,37] and the united-atom simulation results of Ref. [44]. We consider the multiplet as being the smallest building block for the clusters of head groups. The size of a single multiplet is about 3σ, or 1 nm, the distance at which the function $g_{SS}(r)$ drops down to unity for $\lambda=1$. A detailed inspection of Fig. 3 reveals that the positions of the maxima of $g_{SS}(r)$, and hence the multiplet size, do not change noticeably when λ increases from 1 to 5. However, the concentration of head groups inside the multiplets decreases when λ increases. The released head groups then make connections, in

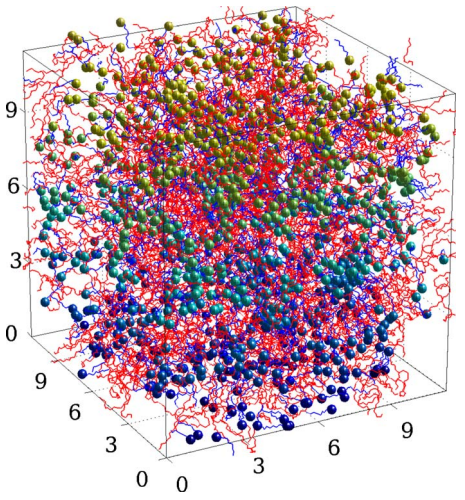

FIG. 2. (Color online) A typical snapshot of the simulated Nafion-like ionomer with a water content $\lambda=5$. Spheres represent the end-group oxygen atoms of side chains. The pendant side chains and backbone chains are drawn by lines (in blue and red correspondingly in online version). Different bead colors correspond to different bead altitudes, with a blue (dark in grayscale) used for low-altitude beads (at the bottom of simulation box) and a yellow (gray in grayscale) used for high-altitude beads (at the top of simulation box). The size of all structural elements is schematic rather than space filling. The box size is 11 nm.

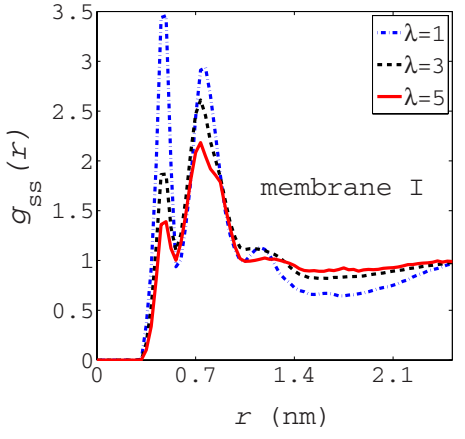

FIG. 3. (Color online) Sulfur-sulfur pair-correlation function $g_{SS}(r)$ for membrane I. Three different water contents: $\lambda=1$: dot-dashed line, $\lambda=3$: dashed line, and $\lambda=5$: full line.

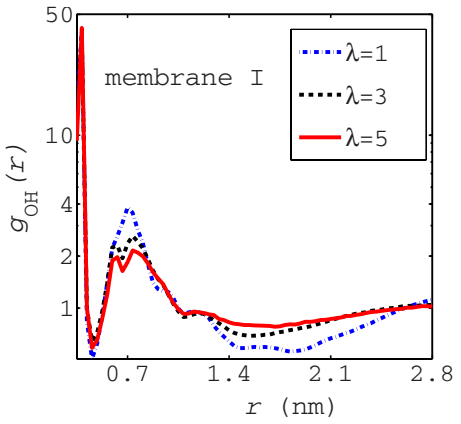

FIG. 4. (Color online) A plot for the head-group oxygen—free proton pair distribution function $g_{OH}(r)$. Three different water contents: $\lambda=1$ dot-dashed line, $\lambda=3$ dashed line, and $\lambda=5$ full line. At higher hydration levels protons are more loosely bound to their host sulfonates. Note that a logarithmic scale is used to accommodate the wide range of $g_{OH}(r)$ into the figure.

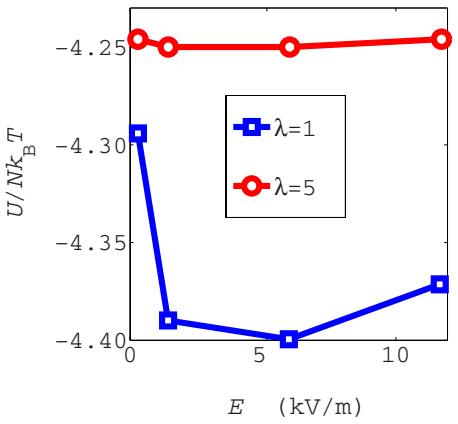

FIG. 5. (Color online) The configurational part of the scaled internal potential energy per monomer, U/Nk_BT, of the membrane II in the presence of weak fields E.

the form of hydrophilic bridges between the multiplets. Such restructuring in the hydrophilic subsystem of the membrane upon absorption of water can be explained in the following manner. At the low value of $\lambda=1$, the multiplets mostly have spherical shapes and are irregularly scattered in the backbone matrix. At the higher value of $\lambda=5$, the multiplet-water mixtures swell and deform into elongated shapes. There is not only a deformation of the swollen cluster, but also a gradual replacement of multiplet sulfonates by water molecules. This effect is seen in Fig. 3 as the lowering of the height of the first peak position of $g_{SS}(r)$ when the water content λ increases from 1 to 5.

The added water does not only change the internal structure of the clusters, but also alters the proton distribution around individual sulfonates. In a highly hydrated membrane, the protons are loosely bound to host sulfonates as a consequence of their strong affinity to water molecules [37].

The oxygen-proton pair distribution function $g_{OH}(r)$ for side chain oxygens and proton counterions is plotted in Fig. 4. The first maximum of $g_{OH}(r)$ at $r\approx 1.1\sigma$ (0.39 nm) corresponds to strongly bound, and thus virtually immobile protons. The area of the distinct second peak of $g_{OH}(r)$ comprises both protons bound to the neighboring oxygens and the unbound protons when $\lambda>1$. The splitting of the second peak of $g_{OH}(r)$ is apparently related to the release of unbound protons in hydrated ionomers. The number of unbound protons can be determined as the difference between the total number of protons inside a single cluster, n_p^c, and the total number of protons close to sulfonates inside the same cluster, n_p^s. The parameter n_p^c can be estimated from the integration of $g_{SS}(r)$ through the relation $n_p^c=(N_S/V)\int_{r=0}^{r=1.4\ \mathrm{nm}} 4\pi r^2 g_{SS}(r)dr$. Then $n_p^s=n_p^c \times (N_S/V)\int_{r=0}^{r=0.4\ \mathrm{nm}} 4\pi r^2 g_{OH}(r)dr$. In doing so we found that: for the case $\lambda=1$ all $n_p^c=17$ protons are bound to sulfonates; for the case $\lambda=3$ there are two unbound protons out of $n_p^c=12$ protons; and finally, for the case $\lambda=5$ there are four unbound protons out of $n_p^c=10$ protons. Thus, the fraction of loosely bound protons increases when more water is absorbed, in agreement with the results of the numerical studies of Ref. [44].

Simulation results for absorbed water, not shown here, indicate that for $\lambda<3$ most of the water molecules are bound to sulfonates. Starting from $\lambda=3$, an increasing number of water molecules gather together inside hydrophilic clusters and show bulklike properties, in agreement with previous studies on the percolation limit for hydrophilic domains [42,45,46].

B. Hydrated membrane in an applied electric field (membrane II)

This subsection is devoted to the morphological changes induced in membrane I by the action of a uniform electric field. In each case, we observe the system until it reaches a steady state, with no further changes in morphology. Such states do not necessarily represent a local or metastable equilibrium, as dissipative processes are still occurring as proton transport currents pass through the material.

First we consider the case of a weak applied electric field, whose strength varies between zero and 12 kV/m. This is the range of fields typically used in experimental studies of bulk transport in PEM materials. The ratio of the internal potential energy of the membrane, defined as the membrane potential energy per monomer without the membrane-field interaction term, to the thermal energy k_BT, is plotted in Fig. 5, and is seen to have little variation with field when $\lambda=5$. At low λ, on the other hand, there is a surprising initial drop in potential energy as the field is applied. This appears to be associated with the release of angular and dihedral tensions left during equilibration of membrane I. Generally speaking, due to the complexity of interactions between the membrane monomers, water molecules, and protons, there are many metastable states separated by energy barriers in the equilibrated membrane. The difference between these metastable states mostly stems from internal stress in the backbone membrane. Applied perturbations such as the external field in our study or raising the membrane temperature in experiments [15–17], are able to drive the system to states with lower energies and internal stresses.

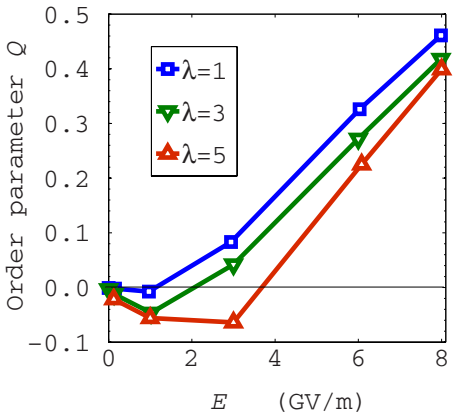

FIG. 6. (Color online) The order-parameter Q [see Eq. (3) in the text] of the head-group dipoles in the membrane II as a function of applied field for three different hydration levels λ.

Experimentalists are familiar with the fact that the final structure of an ionomer membrane is dependent on the method by which it is produced, and that the final form of the material is rarely the configuration with the lowest free energy. Boiling, rinsing, microwave drying, and other thermomechanical steps, as well as the manner of cleaning the membrane of contamination and ridding it of any residual preorientation all influence the membrane structure. Only in the case of higher hydration is the internal stress remaining in membrane I negligibly small. This is an indication of the fact that the water acts as a lubricating influence in determining the membrane morphology. The membrane morphologies corresponding to the initial (membrane I) and field-induced (membrane II) conformations show identical pair correlations, $g_{SS}(r)$, for sulfonates for applied fields below 12 kV/m. This indicates that the increase in internal energy of the low-hydration material seen at fields above 6 kV/m in Fig. 5 is related to the stretching of side chains and backbones caused by field-induced reshaping of the head-group clusters. However, the multiplets that constitute the clusters are not deformed by these weak fields.

It is only at extremely strong fields, of the order of $E \approx 8$ GV/m, that the head-group dipoles start to reorient themselves parallel to the field direction. We can characterize the head-group alignment in terms of a nematic order parameter Q, defined as

$$Q = \frac{1}{2}(3\langle P_z \rangle - 1), \tag{3}$$

where

$$P_z = \frac{1}{N_S}\sum_{i=1}^{N_S} (\hat{\mu}_i \cdot \hat{z})^2, \tag{4}$$

and $\hat{\mu}$ is a unit vector in the direction joining the sulfur to the combined oxygen units in a sulfonate. The angular brackets in Eq. (3) represent statistical averaging during the simulations. The dependence of Q on the applied field E for different hydration levels λ is plotted in Fig. 6.

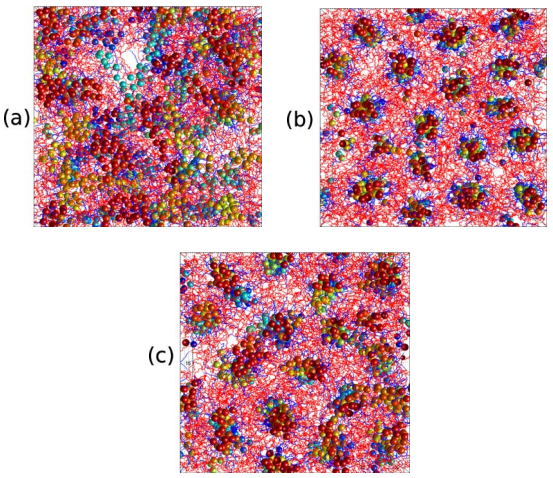

FIG. 7. (Color online) Typical (xy projection) of simulation boxes for λ=3. (a) Membrane I with no applied electric field. (b) Membrane II with applied electric field $E=5$ GV/m. (c) Membrane III with no applied electric field.

This dependence is nonmonotonic, in that the head group ordering first decreases and then increases when the applied field strength is increased. This behavior is most apparent for the highest membrane hydration, λ=5. This reflects the fact that those dipoles already aligned parallel to the field are not strongly affected, but those aligned antiparallel to the field attempt to reorient toward the field direction. The presence of the other dipoles in the cluster at first prevents this, particularly in the cases where there is little water in the membrane, and these dipoles start to rotate away from their original direction. They thus at first become oriented in a direction more perpendicular to the field and this induces a negative value of Q. At very strong fields, however, the dipole-dipole interaction is overcome and the order parameter rapidly increases.

The formation of long-range order in the head-group orientation along the direction of the applied field is accompanied by a related change in membrane morphology. This is seen in the xy projection of the simulation boxes shown in Fig. 7. The isotropic structure of membrane I depicted in Fig. 7(a) is transformed to the hexatic structure of membrane II seen in Fig. 7(b) by the presence of the electric field. This observation is similar to that noted previously for a poled membrane with implicit water [18]. A hexatic phase of hydrophilic clusters with a lattice constant about 2.8–3.5 nm is formed. The walls of these hydrophilic clusters are lined with sulfonates and form cylinders having a diameter of about 1.8 nm, which is close to the simulation results of Ref. [11]. The mean SO_3^--SO_3^- group spacing along the cylindrical cluster is about 0.65–0.80 nm, which is close to the sulfur-sulfur separation distance usually expected for Nafion-like membranes [47].

The flow of protons and the electro-osmotic drag of water molecules [48,49] are limited to the inner area of the rodlike clusters. The membrane conductivities, evaluated using Eqs. (1) and (2), are plotted in Fig. 8. The conductivities have a weak dependence on the applied field for $E<1$ GV/m and are in the range $\chi=1-3$ S/m when λ is varied between 1

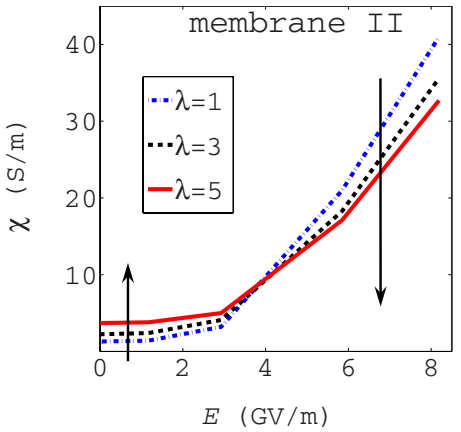

FIG. 8. (Color online) The conductivity χ of membrane II against applied field E for different hydrations λ. The arrows show the direction along which the membrane hydration λ increases.

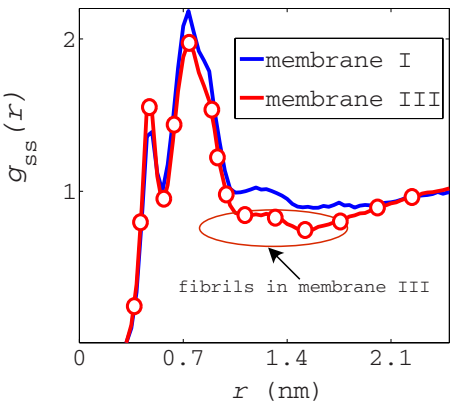

FIG. 9. (Color online) Sulfur-sulfur pair-correlation function $g_{SS}(r)$ for membranes I and III for hydration parameter λ=5. The arrow points to the fibril-like structure of hydrophilic clusters in membrane III.

and 5. These are smaller than the experimentally reported value $\chi=10$ S/m for completely hydrated Nafion with λ =15–25, but are much larger than some theoretical predictions of a conductivity $\chi_S \sim 0.001$ S/m [50]. Figure 8 also confirms the fact that at modest fields absorbed water enhances proton conductivity [46]. We note that the calculated conductivities do not include the Grotthuss mechanism of proton shuttling between water molecules. This issue will be discussed in Sec. IV D.

At high fields, as is evident from Fig. 8, the conductivity $\chi(E)$ is predicted to increase with E. We assume that this nonlinearity in $\chi(E)$ is associated with the emergence of the hexatic structure in the membrane. As seen from Fig. 7, the ordered hydrophilic structure starts to form at applied fields $E_0 \approx 3$ GV/m. Thus the structure of membrane II can be assumed to be isotropic when $E < E_0$ and, accordingly, anisotropic when $E > E_0$. The level of membrane anisotropy grows with E as a consequence of the increased alignment of sulfonate clusters and the decreasing of the tortuosity of the cylindrical channels. Both these factors provide better pathways for protons, and thus increase their mobility. As a result, the proton conductivity increases as a function of the membrane anisotropy, or, equivalently, as a function of the applied field strength E. In addition to inducing long-range ordering in the hydrophilic pathways, the field also polarizes the water absorbed in the membrane. The dielectric saturation of the water consequently restricts the mobility of both water and protons, and thus decreases the conductivity. That is most probably why the membrane conductivity at λ=5 is smaller than the conductivity at λ=1 or 3 in the strongest fields in Fig. 8.

C. Poled hydrated membrane in zero field (membrane III)

It was interesting to note that the membrane did not revert to its isotropic structure when the applied field was removed, but instead retained its hexatic morphology even after lengthy equilibration. In principle, the remnant structure might be metastable and prone to disappear at times longer than the several nanoseconds of simulation time. We accordingly analyzed the time evolution of the total system energy and its electrostatic part and found that the relaxation processes following the release of external load take place during the first several hundred picoseconds of the 2 ns simulations used to relax the membrane. The evolution of the correlation functions g_{SS} and g_{OH} were also monitored and gave the same relaxation time. A snapshot of a poled, relaxed membrane is given in Fig. 7(c). This behavior is similar to the experimental results reported in Ref. [15], where field-induced structures were generated in high-temperature poling experiments on solvent-evaporated ionomers. This phenomenon raises the question of which structure is the more stable and we address this in Sec. V, where we study the free-energy barriers between the isotropic and hexatic morphologies by the method of thermodynamic integration.

The sulfur-sulfur pair distribution functions for membranes I (unpoled) and III (poled) are compared in Fig. 9. The intersulfonate correlations are virtually identical for distances below 3σ (1 nm), showing that the internal structures of the multiplets are unaffected by poling. However, the long-range spatial correlations in membrane III point to an elongation of the membrane clusters along the z axis, a well-known feature of fibril-like formations in hydrophilic clusters. Despite the fact that the morphologies of the two membranes differ macroscopically, the head-group dipoles in each case have no preferential ordering, making the head-group order-parameter Q zero for both membranes.

The pair distribution analysis invoked above is a convenient tool for probing the multiplet structure of clusters, whose dimensions are one nanometer or less. The system morphology on a larger scale, however, is better probed by examining the structure factor. We calculate the partial structure factors of sulfonate oxygens in the xy plane perpendicular to the direction of applied field using the relation

$$S(k_{xy}) = \frac{1}{N_S}\left\langle \sum_i \sum_j \exp(i\mathbf{k}_{xy} \cdot (\mathbf{r}_i - \mathbf{r}_j)) \right\rangle. \quad (5)$$

Here $\mathbf{k}_{xy}$ is the xy component of the wave vector, and $\mathbf{r}_i$ and $\mathbf{r}_j$ are the locations of the sulfonate oxygens, and an average is taken over all directions of $\mathbf{k}_{xy}$. The structure factor for

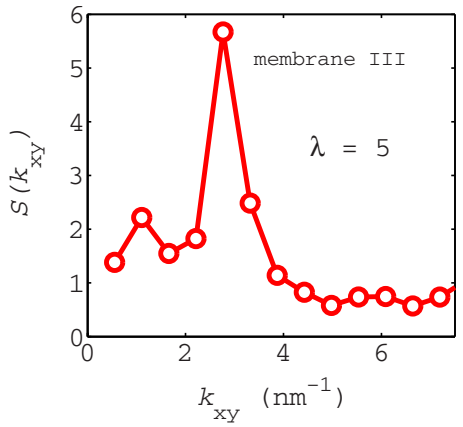

FIG. 10. (Color online) Partial sulfur-sulfur structure factor $S(k_{xy})$ for membrane III. The peak position at $k_{xy}=2.8$ $(\mathrm{nm})^{-1}$ corresponds to the lattice constant 2.0–2.5 nm of the hexatic arrangement of rodlike hydrophilic cylinders. For more details see text.

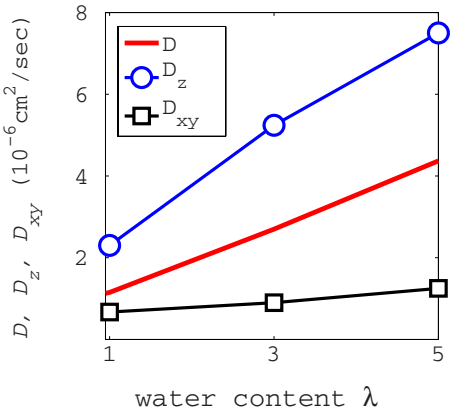

FIG. 11. (Color online) Proton diffusion coefficients for membranes I and III as a function of water content λ. Plain line is for isotropic membrane I with $D=D_z=D_{xy}$. Symbols are for membrane III: circles—D_z and squares—D_{xy}.

membrane III is plotted in Fig. 10. The extent of the nanophase segregation in the membrane is usually deduced from the positions of small-angle peaks of $S(k_{xy})$. The main peak at $k=2.8$ nm^{-1} corresponds to density correlations of sulfonates at length scales of around 2.5 nm. This distance is roughly equal to the lattice constant of the hexatic structure. The primary peak position at $k_{xy}=1.1$ nm^{-1} corresponds to the ionomer peak position observed in scattering experiments [51–53].

D. Diffusion of protons

In this subsection we study proton diffusion in the different membrane morphologies obtained above. Our treatment is restricted to consideration of only the vehicular component of proton (hydronium) diffusion [37], and thus neglects the effects of the Grotthuss mechanism, even though the transport of protons with the help of water molecules is thought to dominate transport in well-hydrated membranes [23,25,54]. Inclusion of the Grotthuss mechanism would require a special treatment of hydrogen bonds such as the empirical valence bond and reactive force field methods that have been developed and successfully applied to small ionomer systems [11,55–58]. The empirical valence bond method of Ref. [57] and the multiscale empirical valence-bond method of Ref. [11] confirm the substantial role of the Grotthuss diffusion when λ is above 5.

In simulations with low water contents $(1<\lambda<5)$, all the water molecules and protons are expected to be confined to the vicinity of sulfonic ions SO_3^- [23]. Recent *ab initio* results for the hydrogen network [59] confirm that at low λ the structural orientation of water in hydrophilic clusters is constrained. Thus the diffusion of protons occurs in a more "vehicular" manner [60], with the protons moving from one sulfonate to another by hopping a typical distance of 0.7–0.8 nm, which is the average separation between SO_3^- sites in humidified Nafion [47]. Proton hopping diffusion is further facilitated by the flexibility of the side chains and the constant rearrangements in position due to their thermal motion [23,47,61,62], and by the high concentration of sulfonates near the channel walls at lower water contents λ [23,25,63].

The partial diffusion coefficients for protons along and perpendicular to the z axis of membrane are calculated using the relations

$$D_z = \frac{1}{2}\lim_{t\to\infty}\frac{\langle|z(t)-z(0)|^2\rangle}{t}, \tag{6}$$

and

$$D_{xy} = \frac{1}{4}\lim_{t\to\infty}\frac{\langle|x(t)-x(0)|^2+|y(t)-y(0)|^2\rangle}{t}. \tag{7}$$

The coefficients D_z and D_{xy} for membranes I and III are plotted in Fig. 11. For the isotropic membrane I the diffusion of protons is also isotropic and $D_z=D_{xy}=D$. The diffusion of protons in membrane III reflects its anisotropic morphology, with D_{xy} being only about 20% of D_z. All the diffusion coefficients increase when more water is absorbed in the membrane [44]. The results for the diffusivity D and the conductivity χ at low fields are related to the carrier density by the Nernst-Einstein relation, $D=\mu k_BT/e=\chi k_BT/(ne^2)$, with μ the carrier mobility and n the number density of the carriers. Putting the low-field values of χ from Fig. 8 and the values of diffusion coefficients D from Fig. 11 into the equation $n=\chi k_BT/(De^2)$, we find that the density of carriers n monotonically increases with the humidity parameter λ. For example, the carrier densities in membrane III increase from $n\approx 0.5n_0$ to $n\approx 0.7n_0$ when λ increases from 1 to 5. Here $n_0=10^{21}$ cm^{-3} and is the average number density of protons in the simulation box. The fraction of protons that remain bound to sulfonates, and thus do not participate in the transport current, is thus least for the most humid membranes.

V. FREE-ENERGY ANALYSIS

While there can be only one absolutely stable form of an ionomer at any given temperature and humidity, various different morphologies may be long lived at normal operating temperatures. As previously mentioned in Sec. IV B, numerous membrane structures can be produced by appropriate treatments, including boiling in water or recasting from wa-

ter solution. It is thus of interest to examine the probable durability of the hexatic structure produced in our simulations by the application of a strong electric field. We have accordingly calculated the free energy of the hexatic material (poled sample, membrane III) and compared it with the free energy of the equilibrium isotropic material (membrane I) produced in our simulations.

Our focus is the Helmholtz free energy, $A=U-TS$, where U is the internal energy of the membrane, T is the absolute temperature, and S is the entropy. The calculation of the internal energy U as a sum of the potential and kinetic energies of all system particles is straightforward. However, the calculation of the entropy of a complex system consisting of the block copolymer monomers, protons, and water, is a challenging task. Various methods based on the evaluation of the entropy from direct molecular dynamics runs have been proposed for simple liquids [64–66]. Unfortunately an adequate generalization of these approaches to ionomeric systems such as Nafion is not possible.

We use the method of thermodynamic integration [67] to evaluate the free-energy difference between the isotropic and remnant hexatic structures. This is achieved by tracing first the free-energy difference $\Delta A_{\mathrm{I}} \equiv A_{\mathrm{I}} - A_{\mathrm{I}}^{0}$ that occurs as the strength of Coulomb interactions U_c^{ij} between charges i and j, which form part of the Hamiltonian H, is gradually reduced to zero in the isotropic structure of membrane I, so that

$$\Delta A_{\mathrm{I}}/(N_S k_B T) = 1/(N_S k_B T) \int_{\nu=0}^{\nu=1} \langle \partial H(\nu)/\partial \nu \rangle d\nu. \qquad (8)$$

Here the coupling parameter ν characterizes the strength of Coulomb interactions U_c^{ij} between charged pairs i and j, where i and j run over membrane head groups, protons and water charges. As a reference system with $\nu=0$ we consider a completely neutral membrane hydrated by a neutral solvent. Although the entropies of the reference system and the simulated system (membrane I) are not known, Eq. (8) describes the free-energy difference between these two membranes. As the coupling parameter ν gradually decreases from 1 to 0, the charges in the simulated membrane decrease and it approaches the reference system. The configurational part of the Hamiltonian $H(\nu)$ was chosen as $U_{\mathrm{conf}}(\nu) = U_{\nu=0}(r) + \nu \Sigma_{i>j} U_c^{ij}$, where the first term $U_{\nu=0}(r)$ is the total potential energy of the ground state of the uncharged membrane. The integrand, $\langle \partial H(\nu)/\partial \nu \rangle$, then reduces to $\langle U_c^{ij}(\nu) \rangle$, which is a smooth function of the coupling parameter ν. A similar evaluation of $\Delta A_{\mathrm{III}} \equiv A_{\mathrm{III}} - A_{\mathrm{III}}^{0}$ was then made for the hexatic structure of membrane III.

The integral (8) was evaluated by decreasing the coupling parameter ν in 20 steps. Precautions were taken to ensure proper equilibration at each step. The same procedure was followed to obtain ΔA_{III}. Our simulations show that at $\nu=0$ the ground states for membranes I and III are identical, making $A_{\mathrm{I}}^{0}=A_{\mathrm{III}}^{0}=A_0$. The calculated excess free energies per sulfonate $\Delta A_i/(N_S k_B T)$, $i=\mathrm{I},\mathrm{III}$, are given in Table I. The difference $\Delta A_{\mathrm{I,III}}=\Delta A_{\mathrm{I}}-\Delta A_{\mathrm{III}}$, plotted in Fig. 12 for different hydration levels λ, determines the stability of respective materials. The difference $\Delta A_{\mathrm{I,III}}$ was found to be positive for all the hydration levels considered. This implies that the hexatic structure found in membrane III is the thermodynamically stable structure. The morphological changes induced by the strong external field thus appear to be irreversible. Its stability is partly based on the difference between the angular and dihedral parts of the potential energy of ionomer polymers ΔU_ϕ and ΔU_θ for membrane I and membrane III, plotted in Fig. 12. We note that the energy difference of $2-6 k_B T$ per sulfonate at water contents $\lambda=1-5$ is not small. For 100 sulfonates the difference between their cylindrical arrangement and a disordered cluster arrangement is several hundred $k_B T$.

TABLE I. The excess Helmholtz free energies per sulfonate, $\Delta A/(N_S k_B T)$, are shown for the initial membrane I and poled membrane III for three different water contents $\lambda=1,3,5$. N_S is the total number of sulfonates SO_3^- in the simulation box.

λ	$\Delta A_{\mathrm{I}}/(N_S k_B T)$	$\Delta A_{\mathrm{III}}/(N_S k_B T)$
1	−265	−271
3	−234	−238
5	−208	−210

VI. CONCLUDING REMARKS

In this paper, we have considered the effects of a field applied in a direction normal to an ionomer membrane and have found that high fields induce a transition to a new structure having an enhanced proton conductivity. In comparison, our previous work on stretched membranes [35] predicted enhanced conductivity in the direction of stretching, which would be in the plane of the film. It is clearly of greater utility to achieve increased transport in the direction normal to the film.

The Nafion poling experiments of Lin *et al.* [15], Middelman *et al.* [16], and Wang *et al.* [17] used solvent cast and annealed membranes above their glass transition temperature. Under these conditions, small fields up to 1 MV/m were

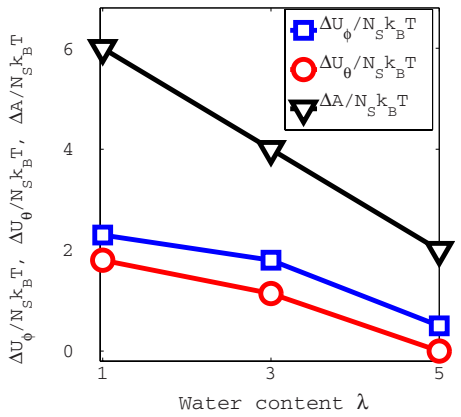

FIG. 12. (Color online) Free-energy difference between initial membrane I and poled membrane III as a function of water content parameter, λ. The contributions from the angular and dihedral parts of the potential energy are also shown.

typically enough to induce oriented morphologies in a system with a high dielectric permittivity. Our test simulations for dilute Nafion solutions indeed show that such small fields push the sulfonates to form elongated filamentary structures. Unfortunately, a direct simulation of large systems with water evaporation and membrane annealing procedures is too demanding of computing resources to be currently feasible.

In systems as complex as humid ionomers, it is not unexpected that there should be several different structures that each represent a local minimum in the free energy and that the barriers to transitions between these morphologies should be much larger than available thermal energies. To achieve a transformation of the ionomer from one morphology to another thus requires either a very long time or else the imposition of a strong perturbation. Because computer modeling is limited to time intervals of at most a few hundred simulated nanoseconds, we chose the route of applying a very strong electric field. The field strengths we used, which were of the order of gigavolts per meter, were larger than can be experimentally sustained in the bulk of an ionomer membrane, and could be found only in the layer adjacent to an electrode. They were, however, sufficient to induce a transformation of the ionomer from its initial isotropic form to an hexatic structure in a few simulated nanoseconds. If the transition processes are governed by Boltzmann factors of the form e^{-V/k_BT}, then the effects of increasing the temperature T should be equivalent to those of reducing the energy barrier V. One of the potentially most significant aspects of the results reported here is the apparent stability of the hexatic phase, as witnessed by its persistence after the field was removed, and by our calculated result that its free energy was lower than that of the isotropic phase.

ACKNOWLEDGMENTS

This work was supported by the U.S. Department of Energy under grant No. DE-FG02-05ER46244 and was made possible by use of facilities at the Case ITS High Performance Computing Cluster and the Ohio Supercomputing Center.

[1] S. M. Haile, Acta Mater. **51**, 5981 (2003).
[2] T. D. Gierke, G. E. Munn, and F. C. Wilson, J. Polym. Sci., Polym. Phys. Ed. **19**, 1687 (1981).
[3] W. Y. Hsu and T. D. Gierke, Macromolecules **15**, 101 (1982); J. Membr. Sci. **13**, 307 (1983).
[4] A. Eisenberg, Macromolecules **3**, 147 (1970).
[5] G. Gebel and O. Diat, Fuel Cells **5**, 261 (2005).
[6] G. Gebel, Polymer **41**, 5829 (2000).
[7] L. Rubatat, G. Gebel, and O. Diat, Macromolecules **37**, 7772 (2004).
[8] L. Rubatat, A. Rollet, G. Gebel, and O. Diat, Macromolecules **35**, 4050 (2002).
[9] A. S. Ioselevich, A. A. Kornyshev, and J. H. G. Steinke, J. Phys. Chem. B **108**, 11953 (2004).
[10] K. Schmidt-Rohr and Q. Chen, Nature Mater. **7**, 75 (2008).
[11] N. P. Blake, M. K. Petersen, G. A. Voth, and H. Metiu, J. Phys. Chem. B **109**, 24244 (2005).
[12] K. Malek, M. Eikerling, Q. Wang, Z. Liu, Sh. Otsuka, K. Akizuki, and M. Abe, J. Chem. Phys. **129**, 204702 (2008).
[13] S. Vorrey and D. Teeters, Electrochim. Acta **48**, 2137 (2003).
[14] Y. Oren, V. Freger, and C. Linder, J. Membr. Sci. **239**, 17 (2004).
[15] H.-L. Lin, T. L. Yu, and F.-H. Han, J. Polym. Res. **13**, 379 (2006).
[16] E. Middelman, Fuel Cells Bull. **2002**, 9 (2002).
[17] Z.-T. Wang, Y.-X. Wang, L. Xu, Q.-J. Gao, G.-Q. Wei, and J. Lu, J. Power Sources **186**, 293 (2009).
[18] E. Allahyarov and P. L. Taylor, Phys. Rev. E **80**, 020801(R) (2009).
[19] S. Nemat-Nasser, J. Appl. Phys. **92**, 2899 (2002).
[20] K. J. Chae, M. Choi, F. F. Ajayi, W. Park, I. S. Chang, and I. S. Kim, Energy Fuels **22**, 169 (2008).
[21] A. A. Franco, P. Schott, C. Jallut, and B. Maschke, J. Electrochem. Soc. **153**, A1053 (2006).
[22] E. T. Enikov and G. S. Seo, Exp. Mech. **45**, 383 (2005).
[23] E. L. Thompson, T. W. Capehart, and T. J. Fuller, J. Electrochem. Soc. **153**, A2351 (2006).
[24] M. N. Tsampas, A. Katsaounis, and C. G. Vayenas, Electrochim. Acta **51**, 2743 (2006).
[25] P. Choi, N. H. Jalani, and R. Datta, J. Electrochem. Soc. **152**, E123 (2005).
[26] A. Vishnyakov and A. V. Neimark, J. Phys. Chem. B **105**, 7830 (2001); **105**, 9586 (2001).
[27] S. Yamamoto, R. Jinnouchi, Sh. Yamakawa, and Sh. Hyodo, 14th International Conference on the Properties of Water and Steam, Kyoto, Japan, 2004 (unpublished), Vol. 411.
[28] E. Allahyarov and P. L. Taylor, J. Chem. Phys. **127**, 154901 (2007).
[29] S. Yamamoto, R&D Rev Toyota CRDL **38**, 10 (2003).
[30] K. Malek, M. Eikerling, Q. Wang, T. Navessin, and Z. Liu, J. Phys. Chem. C **111**, 13627 (2007).
[31] J. T. Wescott, Y. Qi, L. Subramanian, and T. W. Capehart, J. Chem. Phys. **124**, 134702 (2006).
[32] L. Pisani, M. Valentini, D. H. Hofmann, L. N. Kuleshova, and B. D'Aguanno, Solid State Ionics **179**, 465 (2008).
[33] S. J. Paddison and T. A. Zawodzinski, Solid State Ionics **113-115**, 333 (1998).
[34] M. W. Mahoney and W. L. Jorgensen, J. Chem. Phys. **112**, 8910 (2000).
[35] E. Allahyarov and P. L. Taylor, J. Phys. Chem. B **113**, 610 (2009).
[36] D. Brandell, J. Karo, A. Liivat, and J. O. Thomas, J. Mol. Model. **13**, 1039 (2007).
[37] A. Venkatnathan, R. Devanathan, and M. Dupuis, J. Phys. Chem. B **111**, 7234 (2007).
[38] M. Mazars, J. Chem. Phys. **115**, 2955 (2001).
[39] D. Rivin, G. Meermeier, N. S. Schneider, A. Vishnyakov, and A. V. Neimark, J. Phys. Chem. B **108**, 8900 (2004).
[40] S. C. Glotzer and W. Paul, Annu. Rev. Mater. Res. **32**, 401 (2002).

[41] M. Eikerling, A. A. Kornyshev, and U. Stimming, J. Phys. Chem. B **101**, 10807 (1997).
[42] K. A. Mauritz and R. B. Moore, Chem. Rev. **104**, 4535 (2004).
[43] D. Moilanen, I. Piletic, and M. D. Fayer, J. Phys. Chem. C **111**, 8884 (2007).
[44] See S. Cui, J. Liu, M. E. Selvan, D. J. Keffer, B. J. Edwards, and W. V. Steele, J. Phys. Chem. B **111**, 2208 (2007) and references therein.
[45] J. Fimrite, H. Struchtrup, and N. Djilali, J. Electrochem. Soc. **152**, A1804 (2005).
[46] Z. Lu, G. Polizos, D. D. Macdonald, and E. Manias, J. Electrochem. Soc. **155**, B163 (2008).
[47] S. Tanimura and T. Matsuoka, J. Polym. Sci., Part B: Polym. Phys. **42**, 1905 (2004).
[48] M. Laporta, M. Pegoraro, and L. Zanderighi, Phys. Chem. Chem. Phys. **1**, 4619 (1999).
[49] D. Kim and E. Darve, Phys. Rev. E **73**, 051203 (2006).
[50] K. Chan, Y. W. Tang, and I. Szalai, Mol. Simul. **30**, 81 (2004).
[51] S. S. Jang, V. Molinero, T. Cagin, and W. A. Goddard III, J. Phys. Chem. B **108**, 3149 (2004).
[52] S. K. Young and K. A. Mauritz, J. Polym. Sci., Part B: Polym. Phys. **39**, 1282 (2001).
[53] S. K. Young, S. F. Trevino, and N. C. Tan, J. Polym. Sci., Part B: Polym. Phys. **40**, 387 (2002).
[54] I. H. Hristov, S. J. Paddison, and R. Paul, J. Phys. Chem. B **112**, 2937 (2008).
[55] S. Walbran and A. A. Kornyshev, J. Chem. Phys. **114**, 10039 (2001).
[56] E. Spohr, A. A. Kornyshev, and P. Commer, J. Phys. Chem. B **106**, 10560 (2002).
[57] D. Seeliger, C. Hartnig, and E. Spohr, Electrochim. Acta **50**, 4234 (2005).
[58] D. W. M. Hofmann, L. Kuleshova, and B. D'Aguanno, J. Mol. Model. **14**, 225 (2008).
[59] R. Devanathan, A. Venkatnathan, and M. Dupuis, J. Phys. Chem. B **111**, 8069 (2007).
[60] S. J. Paddison and R. Paul, Phys. Chem. Chem. Phys. **4**, 1158 (2002).
[61] P. Commer, A. G. Cherstvy, E. Spohr, and A. A. Kornyshev, Fuel Cells **2**, 127 (2002).
[62] S. Dokmaisrijan and E. Spohr, J. Mol. Liq. **129**, 92 (2006).
[63] M. Saito, K. Hayamizu, and T. Okada, J. Phys. Chem. B **109**, 3112 (2005).
[64] S. Do Hong and M. Shik Jhon, Chem. Phys. Lett. **273**, 79 (1997).
[65] S. Do Hong and D.-J. Jang, Chem. Lett. **31**, 946 (2002).
[66] S. D. Hong, H.-C. Shin, and K.-H. Cho, Bull. Korean Chem. Soc. **26**, 1673 (2005).
[67] J. G. Kirkwood, J. Chem. Phys. **3**, 300 (1935).